Electronic Supplementary Material (ESI) for Nanoscale.

Synergetic Effects of Fe^{3+} doped Spinel $Li_4Ti_5O_{12}$ Nanoparticles on Reduced Graphene Oxide for High Surface Electrode Hybrid Supercapacitors

Supplementary document

Sergej Repp[1], Ersan Harputlu[2], Seda Gurgen[1,2], Mike Castellano[1], Nora Kremer[1], Nils Pompe[1], Jakob Wörner[1], Anke Hoffmann[3], Ralf Thomann[3], Fatih M. Emen[4], Stefan Weber[1,5], Kasim Ocakoglu[2,6], Emre Erdem[1,§,*]

[1]Institut für Physikalische Chemie, Albert-Ludwigs-Universität Freiburg, Albertstr. 21, 79104 Freiburg im Breisgau, Germany. [2]Advanced Technology Research & Application Center, Mersin University, Ciftlikkoy Campus, TR-33343 Mersin, Turkey. [3]Freiburger Materialforschungszentrum – FMF, Stefan-Meier-Straße 21, 79104 Freiburg im Breisgau, Germany. [44]Faculty of Arts and Sciences, Department of Chemistry, Mehmet Akif Ersoy University, Burdur, Turkey. [5]Freiburg Institute of Advanced Studies-FRIAS, Albert-Ludwigs-Universität Freiburg Albertstraße 19, 79104 Freiburg im Breisgau. [6]Department of Energy Systems Engineering, Faculty of Technology, Mersin University, TR-33480 Tarsus, Mersin, Turkey.

*e-mail: emre.erdem@physchem.uni-freiburg.de.

[§]present address: GREMAN UMR 7347, Université de Tours, CNRS, INSA-CVL, 16 rue Pierre et Marie Curie, 37071 Tours, France

Keywords: Hybrid Supercapacitor, Spinel $Li_4Ti_5O_{12}$, Electron Paramagnetic Resonance, Electrochemical impedance spectroscopy

Synthesis of sLTO/rGO-composite

The chemicals used for the synthesis of rGO are listed in the **table S1**.

Table S1: Chemicals used during the synthesis of rGO , Fe:sLTO and rGO/sLTO compounds.

Chemicals	Formula	Producer Company
Graphite flakes (natural, 99.8%)	C	Alfa Aesar
Sodium nitrate	$NaNO_3$	AnalaR Normapur VWR Prolabo
Sulfuric acid (97-99%)	H_2SO_4	AlliedSignal Riedel-de Häen
Potassium permanganate (99.0%)	$KMnO_4$	AnalaR Normapur VWR Prolabo
Hydrogen peroxide (30%	H_2O_2	Chemsolute

(stab.) p.A.)		
Hydrochloric acid (≥ 37%)	HCl	Sigma Aldrich
Ethanol (absolute)	EtOH	AnalaR Normapur
Phosphoric acid (85%)	H_3PO_4	Merck
Titanium isopropoxide (99.999%) trace metal	$Ti(OCHMe_2)_4$	Sigma-Aldrich
Ferric nitrate (99.95%, trace metals)	$Fe(NO_3)_2 \cdot 9H_2O$	Sigma-Aldrich
L-Ascorbic acid (≥ 99% p.a.)	$C_6H_8O_6$, L-AA	Carl Roth
Benzyl alcohol (≥ 98.0%)	C_7H_8O	Carl Roth
Lithiumhexafluorophosphate	$LiPF_6$	Sigma Aldrich (0.1 M, ethylene carbonate/ethyl methyl carbonate, 50/50 (v/v))

Synthesis of the graphene oxide (GO)

The rGO samples were synthesized by different modified Hummers methods [1]. Namely, route A: natural flakes (0.618 g, 1 wt%), $NaNO_3$ (0.543 g), H_2SO_4 (97-99%, 23 mL) and $KMnO_4$ (2.985 g, 5 wt%) and 5 wt% $KMnO_4$ %) were mixed in an ice bath under strong magnetic stirring. At 2 h of the exothermic oxidation reaction, the black-green reaction mixture was stirred at room temperature (RT) for further 50 h. During the stirring, an increase of viscosity as well as a slow colour change from black-green to brown-orange has been observed. The reaction mixture has been diluted with deionized water (46 mL) and heated at 90 °C for 1.5 h. After cooling down to RT, H_2O_2 (30%, 10 mL) was added to the light brown-orange reaction mixture to neutralize unreacted $KMnO_4$. The oxidized graphite was washed with HCl (1M, 25 mL) followed by centrifugation (2500 rpm, 10 min). For further purification, the light brown solid was washed with a H_2O/EtOH-mixture (1:5, 18 mL) and centrifuged (4000 rpm, 15 min) again. The synthesized solid was dispersed in deionized water (160 mL), sonicated for 2 h and centrifuged (4000 rpm, 10 min). Finally, to improve the exfoliation of the black graphene oxide, the sample was sonicated for another 2 h.

This method (route A) was modified to find more efficient, faster and ecologically friendly way for obtaining battery grade rGO in a possible industrial scale. The route B differs in the decreased amount of $KMnO_4$ to 4 wt% and extended reaction time for over 12 h instead of heating it at 90 °C for 1.5 h. In the route C, $NaNO_3$ was replaced by 85 % phosphoric acid (H_3PO_4) because of ecological and safety reasons. Instead, graphite flakes (0.506 g, 1 wt%), $KMnO_4$ (3.264 g, 6 wt%) and H_2SO_4 / H_3PO_4 (9:1, 66ml) -mixture was strongly stirred ice bath for 3 hours. The ice bath was replaced by oil bath and the black green solution was heated to 48 °C for 17 h. During the stirring, an increase of viscosity as well as a slow color change to brown has been observed. Unreacted $KMnO_4$ was removed in an exothermic reaction by adding a H_2O/H_2O_2-mixture (9:1, 100 mL) under ice bath conditions and the high acid reaction mixture (pH-value < 0.5) stirred at RT overnight. To remove water soluble impureness, the reaction mixture was washed several times by centrifugation (4000 rpm, 45 min). For further purification, the oxidized graphite was washed with deionized water (160 mL), HCl (1M, 100 mL) and EtOH (2 times, 200 mL) followed by centrifugation (4000 rpm, 1 h) for 4 times. Finally, the synthesized graphene oxide was dispersed in deionized water (dH_2O, 160 mL). The route D, differs from the route C only in the further chemical reduction process. All samples were characterized with the standard (XRD, UV-Vis, TEM, SEM, TGA) and advanced (CW-EPR, Raman, ATR-TFIR) methods (for detailed analysis see supplementary document). The quality of rGO samples were evaluated in terms of layer thickness from absorbance experiments, the amount of oxidized carbon groups by EPR experiments. Also, the spinel phase purity of LTO and their crystalline size of ~50 nm in diameter was obtained by the Scherrer equation from the XRD analysis.

Synthesis of $Li_4Ti_5O_{12}$ and Fe^{3+} doped $Li_4Ti_5O_{12}$ NPs were obtained as follows:

Benzyl alcohol (BA, 6.5 ml) and dH_2O (2.5 ml) were mixed and the solution stirred in an ice bath. Titanium isopropoxide (2.0 ml) was dissolved in EtOH (10 ml) and slowly dropped into the previous mixture. After stirring for 2 h, the precipitates were vacuum-filtered, washed in EtOH and dried in a drying oven at 60 °C for 12 h. Then, it was dispersed in a Li_2CO_3 (0.1 M) aqueous solution. After stirring for 30 min, the suspension was transferred into a Teflon-lined stainless steel autoclave, sealed and kept at 80 °C for 10 h. The white precipitate was separated by centrifugation, washed with dH_2O several times to remove an excess of impurities before drying at 60 °C for 12 h. Subsequently, the white powder was calcinated at 800 °C for 3 h in an inert atmosphere to obtain $Li_4Ti_5O_{12}$. Fe^{3+} doped $Li_4Ti_5O_{12}$ NPs was also synthesized in the same manner, briefly: Ferric nitrate ($Fe(NO_3)_2{\cdot}9H_2O$) solutions in different molar concentrations as iron source were prepared (0.001 mol% Fe^{3+}, 0.01 mol% Fe^{3+}, 0.1 mol% Fe^{3+}, 0.5 mol% Fe^{3+}, 1 mol% Fe^{3+}, 2 mol% Fe^{3+}, 5 mol% Fe^{3+}). Then, 100 µl of each ferric nitrate solution was added to the mixture of precursor solution of $Li_4Ti_5O_{12}$ (6.5 ml BA, 2.5 ml H_2O and 2.0 ml titanium isopropoxide. All subsequent experimental steps were conducted in a similar manner to $Li_4Ti_5O_{12}$.

Synthesis of sLTO/rGO-composite (chemical reduction of GO)

Route A: the obtained GO-water suspension (340 ml) was mixed with sLTO (1.08 g) and L-Ascorbic acid (L-AA, 5.02g) under magnetic stirring in an ice bath. After stirring at RT for three days, it was observed that the color of the acid reaction mixture (pH-value = 1.5) has changed from light brown to black, which is a clear indication that the reduction of GO was successful. The purification of the synthesized sLTO/rGO-composites was achieved by washing the two product-fractions with deionized water (4 times, all in all 730 mL) and centrifugation (4000 rpm, 15 min, 5 times). After drying at 80 °C for 1.5 days in the drying oven and mortaring, the reunited reaction product was obtained as a dark grey powder (2.813 g). The reduction process of routes B and C were performed in the same way like in the route A. The reduction process of route D was adopted from Fathy *et al.* [2] Briefly, the previously synthesized GO-dispersion (160 mL) was sonicated for 1h, diluted with deionized water (100 mL) and afterwards mixed with LTO (1.072 g) and L-AA (9.949 g). The reaction mixture was heated at 80°C and stirred at this temperature for 1.5 h. After a light increase in viscosity as well as a colour change from light brown to black was observed, which is a clear indication that the reduction of GO was successful, the acid reaction mixture (pH-value = 2.0) was stirred at RT for another 2.5 h. The purification of the synthesized LTO/rGO-composites was achieved by washing the two product-fractions with deionized water (3 times, all in all 529 mL) and centrifugation (5000 rpm, all in all 4 h, 3 times). After drying at 80 °C for 1 day in the drying oven and mortaring, the reaction product was obtained as a light grey powder (1.277 g).

Conventional reduction process with L-AA route (A, B, C)

The sLTO/rGO-composites were synthesized using a conventional reduction process with L-AA. [2] The previously synthesized GO-dispersion (340 mL) and afterwards mixed with sLTO (1.082 g) and L-AA (5.017 g) under magnetic stirring in an ice bath. After stirring at RT [3] for three days, it was observed that the colour of the acid reaction mixture (pH-value = 1.5) has changed from light brown to black, which is a clear indication that the reduction of GO was successful. The purification of the synthesized sLTO/rGO-composites was achieved by washing the two product-fractions with deionized water (4 times, all in all 730 mL) and centrifugation (4000 rpm, 15 min, 5 times). After drying at 80 °C for 1.5 days in the drying oven and mortaring, the reunited reaction product was obtained as a dark grey powder (2.813 g).

Aggressive reduction process with L-AA route (D)

The sLTO/rGO-composites were synthesized using an aggressive reduction process with L-AA The previously synthesized GO-dispersion (160 mL) was sonicated for 1 h, diluted with deionized water (100 mL) and afterwards mixed with sLTO (1.072 g) and L-AA (9.949 g). The reaction mixture was heated at 80°C and stirred at this temperature for 1.5 h. After a light increase in viscosity as well as a colour change from light brown to black was observed, which is a clear indication that the reduction of GO was successful, the acid reaction mixture (pH-value = 2.0) was stirred at RT for another 2.5 h. The purification of the synthesized LTO/rGO-composites was achieved by washing the two product-fractions with deionized water (3 times, all in all 529 mL) and centrifugation (5000 rpm, all in all 4 h, 3 times). After drying at 80 °C for 1 day in the drying oven and mortaring, the reaction product was obtained as a light grey powder (1.277 g).

Continuous Wave-Electron Paramagnetic Resonance Spectroscopy (CW-EPR)

CW-EPR measurements were performed understand the electronic environment of unpaired electrons, thus spins, on the rGO-surface as well as the purity of the synthesized sLTO/rGO-composites. The CW-EPR spectra were recorded at RT with a Bruker EMX spectrometer. Data processing was carried out with the software WIN-EPR® (Bruker).

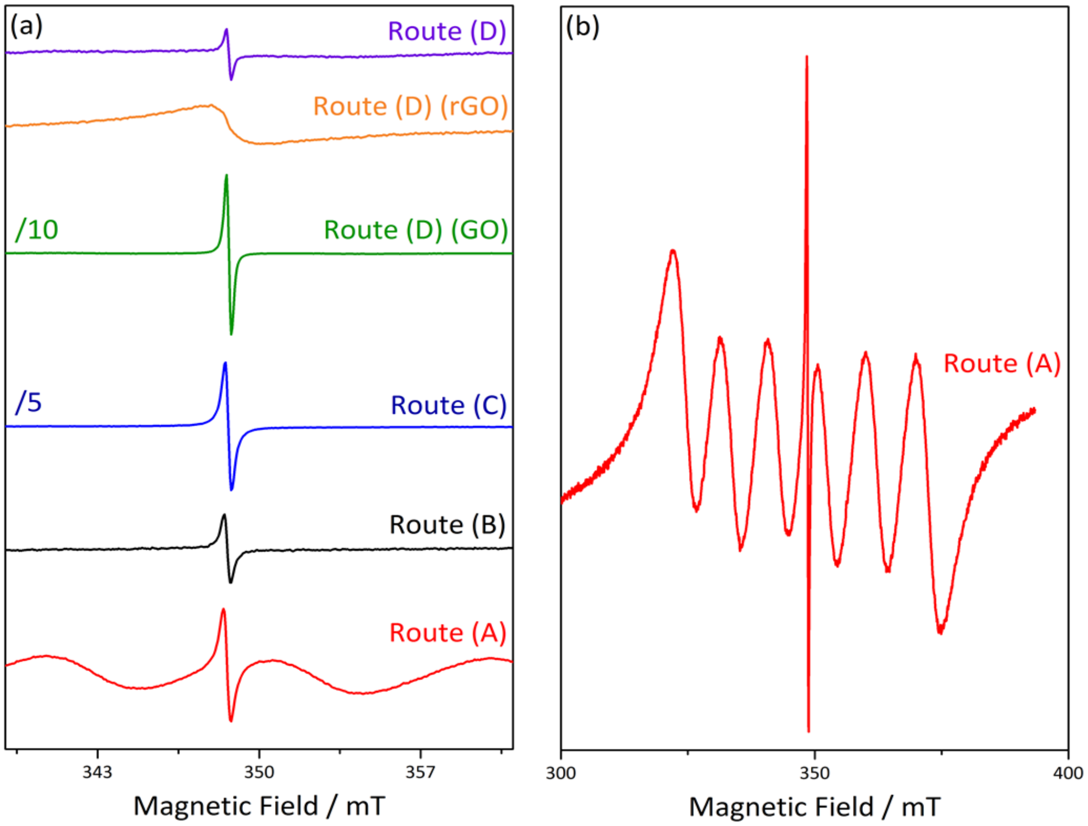

Figure S1: (a): Comparison of the EPR spectra of the undoped rGO/LTO obtained from the Routes (A), (B), (C) and (D). (b): EPR spectrum of Route A, measured by broader magnetic scan range and allows the hyperfine splitting resolving of the Mn^{+2} ion.

(A) containing the characteristic six-line signal of manganese.

The g_e-factor is defined for free electrons with a value of 2.0023 (**Equation 4**). However, this value can vary due to the influence of magnetic interactions, involving the orbital angular momentum of the unpaired electron, as well as the chemical environment. [4,5] For instance in organic radicals, the magnetic moment is suppressed as far as possible, so that the measured g-value is similar to the one of free electrons mentioned above.

Table S2: Summary of the measurement conditions and the calculated g-factor-values.

Route	**Frequency / MHz**	**B_0 / mT**	**Attenuation range / dB**	**Quality factor Q**	**Receiver gain**	**g-factor**
(A)	9.773364	348.60	20	2100	10^3	2.0031
(B)	9.773346	348.65	20	2500	10^3	2.0028
(C)	9.776050	348.70	20	1100	10^3	2.0031
(D) (GO)	9.776050	348.75	20	1100	10^3	2.0028
(D) (rGO)	9.775312	348.70	20	1600	10^3	2.0029

(D)	9.776050	348.75	20	1100	10^3	2.0028

As a result of the different chemical environment, the variation of g-value can be used to determine the nature of the involved radicals by EPR spectroscopy. Carbon-centred radicals for example would be close to the value of g_e whereas oxygen-centred radicals would have g-values > 2.004. [5–8] During the reduction process, a transfer from oxygen-centred to carbon-centred radicals can be observed, so that theoretically the g-value of GO should decrease simultaneous with the amount of oxygen-centred radicals. [5]

Applying this knowledge on the synthesized sLTO/rGO-composites (**Table S2**), it can be proven that the majority of the radicals contained in the respective samples are carbon-centred.

Another observation by comparing the presented EPR spectra in **Figure S1** (a) and (b) is the characteristic six-line signal around g = 2.0000 of Mn^{2+} paramagnetic ions which is only observable for Route (A). [5] Manganese residues of the oxidation process cannot be completely eliminated during the washing process, so that these signals should normally be visible in EPR spectra if permanganate was used for the oxidation process. The fact that these signals are missing for all samples except for Route (A) is assumed to be originated in manganese amounts below the detection level of EPR. [5]

Thermogravimetric/Differential thermal analysis (TG/DTA)

TG measurements were performed to determine the composition of the synthesized sLTO/rGO-mixture. TG measurements were recorded with a Seiko SII TG/DTA 7200 instrument at a heating rate of 10 °C min^{-1} under a N_2 flow of 250 ml min^{-1}.

In Figure 10 (a), three major weight losses areas can be observed for all four analysed sLTO/rGO-composites. The first of these regions is assigned to 20-100 °C and can be attributed to the endothermic loss of intercalated water leavings (**Figure S2** (b)). [9] The presented TGA curves (**Figure S2** (a)) thereby show that Route (A) still possesses an elevated amount of water leavings (~ 28 %). In contrast, the water content of the other Routes is much less significant (~ 1-3 %).

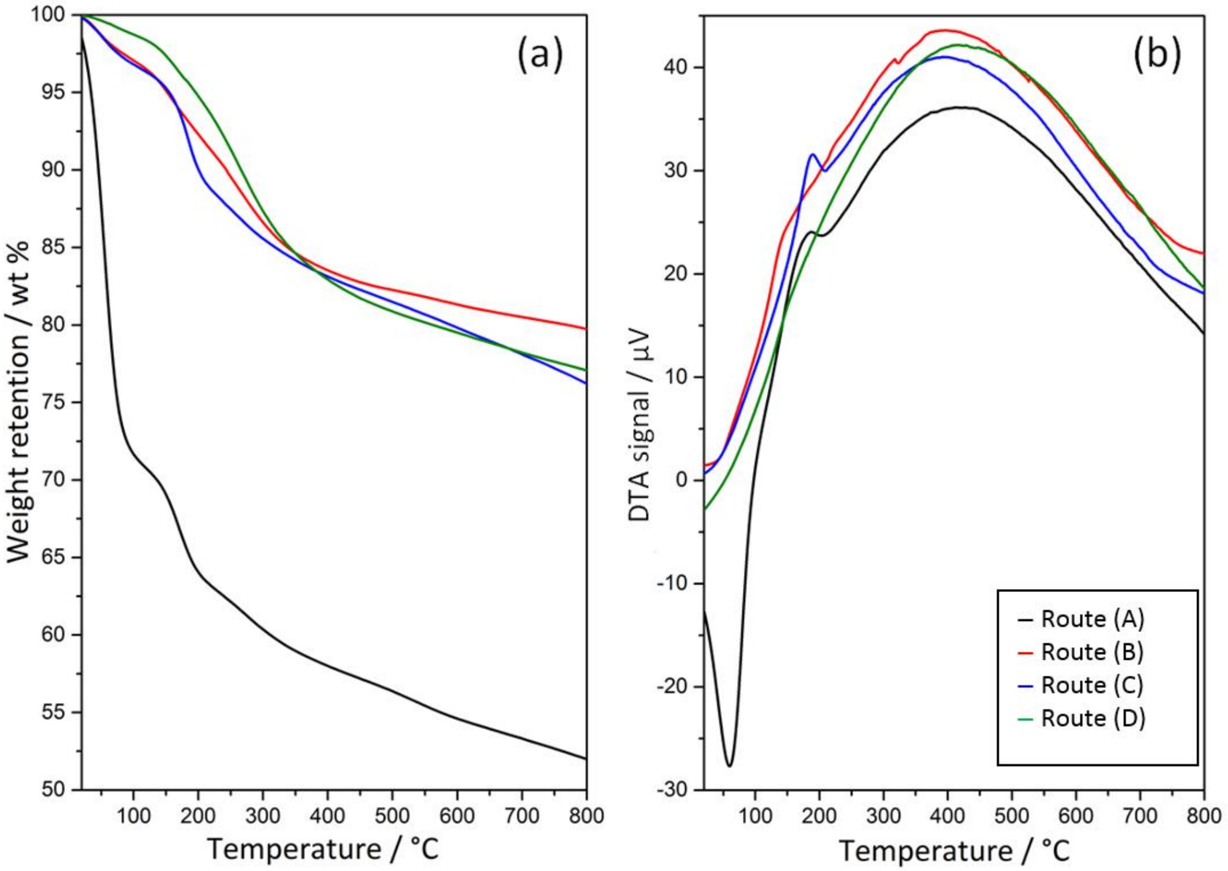

Figure S2: (a): Comparison of the TGA plots of (black curve), (red curve),

(blue curve) and (green curve). (b): Comparison of the DTA plots of Route (A),

Route (B), Route (C) and Route (D).

The second weight loss is about 150-220 °C and is assumed to be originated in the exothermic decomposition of labile oxygen functionalities (Figure 10 (b)) into CO, CO_2 and steam. [2,9–12] The correspondent weight loss of Route (A) and (C) is only ~ 5 % (Figure 10 (a)) which proves the high effectiveness of the reduction process. The weight loss of Route (B) and (D) (~ 3 %) is even lower than the one observed for the Routes (A) and (C).

UV-VIS Spectroscopy (UV-VIS)

UV-VIS measurements of the synthesized GO-dispersions were performed to analyse their respective absorbance qualities as well as their purity. The UV-VIS spectra were recorded at RT with a SHIMADZU UV-2450 UV-VIS spectrometer with a measurement wavelength range of 190-900 nm (single monochromator: high-performance blazed holographic grating in aberration-corrected Czerny-Turner mounting) and a resolution of 0.1 nm. Data processing was carried out with the software UVProbe.

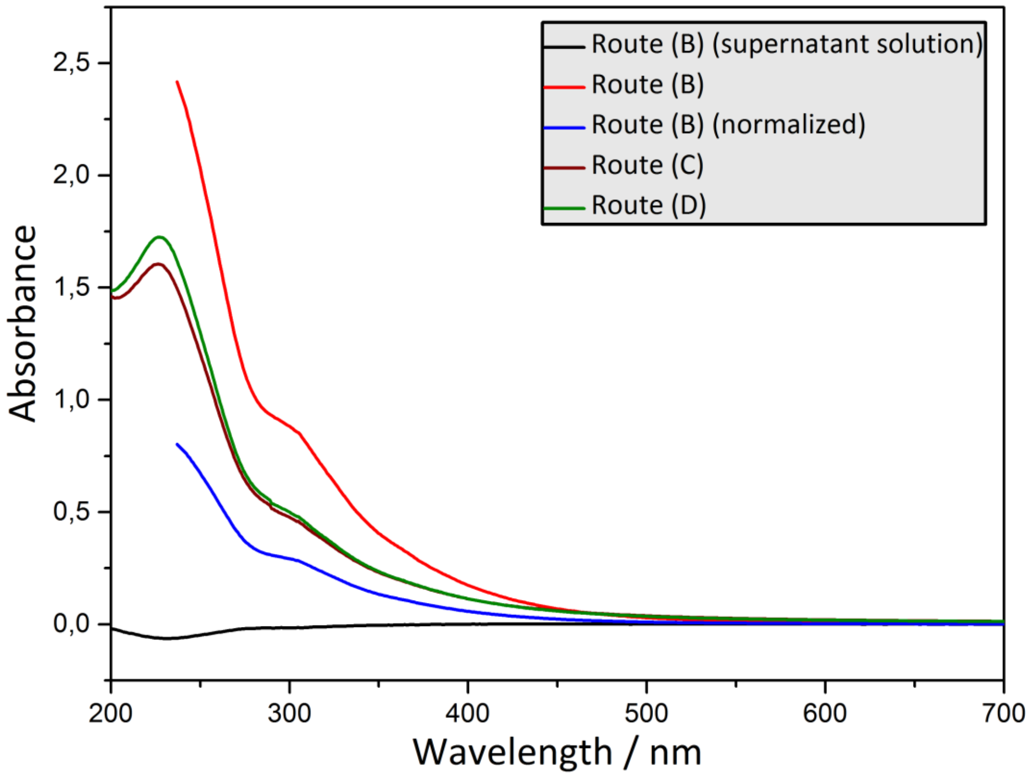

Figure S3: UV-VIS spectra of aqueous GO dispersions synthesized by different methods. Route (B) (supernatant solution) represents the curve of the supernatant orange solution tipped away during the washing process of Route (B). Route (B) (normalized) illustrates the curve of the baseline-normalized Route (B).

By treating all *sp*^{2} clusters as a single phenyl ring, the variation of the optical absorption intensity near 230 nm can directly be linked to the amount of potassium permanganate used during the synthesis. [13] A higher mass ratio of potassium permanganate would lead to a higher number of linking chromophore units and as a result to thinner GO-layers. [13] As a consequence of this relation, the UV-Vis spectroscopy represents a convenient method to determine the number of GO-layers based on the amount of potassium permanganate used for the oxidation process and the optical absorption intensity of the π-π* plasmon peak near 230 nm.

In addition, it could have been shown that both oxidation methods seem to deliver a similar quality of synthesized graphene oxide, so that the application of the recent developed, more ecological GO-synthesis method would be preferred in the future.

Applying this knowledge on the absorption curves for the different Routes, the expectations are that the spectra of the Routes (C) and (D) should be nearly identical, which could be demonstrated in **Figure S3**. Furthermore, the π-π* plasmon peak observed for Route (C) and (D) should be more intensified than the same peak representing Route (B). However, this last assentation could not have been proven due to another factor with a wide influence on the absorption capability of the GO-samples; the concentration of the dispersed GO.

The results of the more concentrated analysis sample of Route (B) were baseline-normalized to make them comparable to the other curves. By comparing the resulting data (Figure 4) to Route (C), respectively Route (D), the expectations that an elevated amount of potassium permanganate would lead to a more intensified π-π* plasmon peak at ~ 230 nm could be satisfied. Furthermore, it could be shown that the ecological GO-synthesis used for Routes (C) and (D) delivers reproducible results.

X-Ray Diffraction (XRD)

XRD measurements were performed to identify the structure and analyse the purity of the synthesized sLTO/rGO-mixture. The XRD patterns were recorded with a STADIP powder diffractometer (Stoe & Cie GmbH, Darmstadt) in transmittion geometry with a Cu-$K_{\alpha}1$ radiation source (Ge-(111)-monochromator) and an image plate detector in the scan range of 5° to 120° (angular resolution of 0.02°) at a wavelength of λ = 0.154 nm. The preparation of the samples was performed by using a polyvinyl acetate film and special glue based on isoamyl alcohol instead of the typically used "Scotch-Magic Tapes" technique.

Applying XRD on the synthesized sLTO/rGO-composites, it becomes clear that their expected reflection peaks must be very similar to the ones of the crystalline LTO spinel. The only difference to the XRD pattern of pure sLTO must consist in an almost undetectable, broad reflection peak at ~ 26° which is related to the amorphous rGO phase. [14] By comparing the four samples of the Routes (A), (B), (C) and (D) presented in Figure 5 to the pure sLTO nanopowder used for the synthesis, as well as the literature data of sLTO, the assumption above could have been totally approved due to the perfect overlapping of the respective reflection peaks. The only difference to the pure sLTO nanopowder consists in the intensity of the reflection peaks, which is a consequence of the amorphous rGO contained in the synthesized samples. Furthermore, it seems like the synthesized sLTO/rGO-composites contain impurities of unreacted, crystalline graphite due to a slim, weak reflection peak for all the samples at ~ 28°. The little bump at around 55° in the sample patterns is estimated to be originated in the impreciseness of the background extinguishing. Due to the usage of potassium permanganate for the oxidation process, it was expected to observe weak reflection peaks of MnO leavings in the XRD patterns. The absence of these signals is estimated to be originated in MnO amounts below the detection level of XRD.

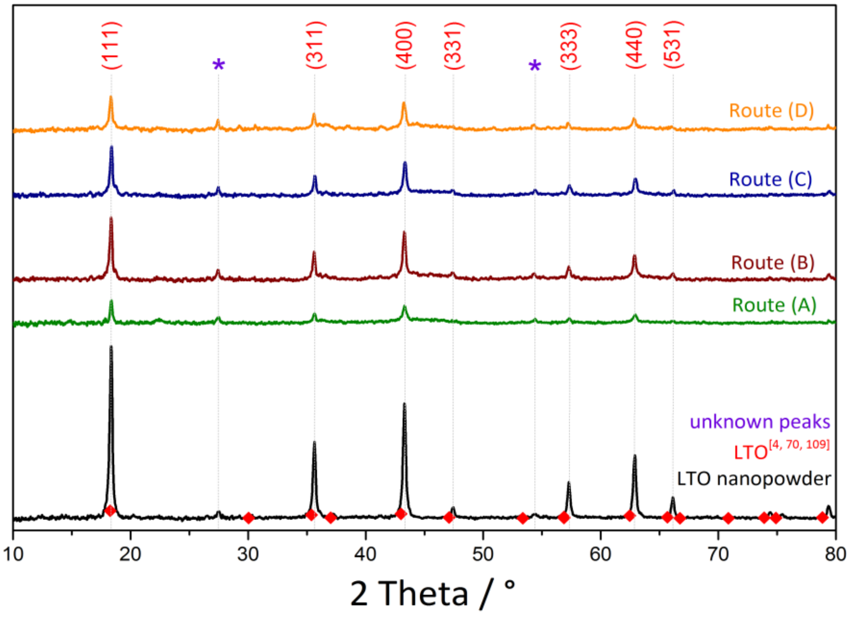

Figure S4: Comparison of the XRD patterns of the synthesized sLTO/rGO-composites with sLTO nanopowder and literature data of sLTO. [15–17]

Table S3: Particle size of the crystalline sLTO nanoparticles by Scherrer equation.

Route	$\boldsymbol{d_{(111)}}$ **/ nm**	$\boldsymbol{d_{(311)}}$ **/ nm**	$\boldsymbol{d_{(400)}}$ **/ nm**	$\boldsymbol{d_{(331)}}$ **/ nm**	$\boldsymbol{d_{(333)}}$ **/ nm**	$\boldsymbol{d_{(440)}}$ **/ nm**	$\boldsymbol{d_{(531)}}$ **/ nm**	$\boldsymbol{d_{\mathrm{average}}}$ **/ nm**
(A)	68.1(5)	48.1(8)	46.9(5)	3.4(9)	52.8(8)	34.0(5)	61.8(9)	45.0(5)
(B)	54.2(5)	57.7(8)	59.6(5)	3.4(9)	45.6(8)	40.9(5)	51.5(9)	44.7(5)
(C)	53.5(5)	58.0(8)	56.3(5)	3.7(9)	46.7(8)	46.8(5)	75.2(9)	48.6(5)
(D)	46.0(5)	9.7(8)	53.4(5)	3.9(9)	50.9(8)	54.8(5)	5.4(9)	32.0(5)

The LTO particle size *d* of the analysed XRD patterns (**table S3**) can be determined from the full width at half-maximum (FWHM) of the reflection peaks by applying the well-known Scherrer equation (Eq. 1): [3,18,19]

$$d = \frac{K \cdot \lambda}{\beta \cdot \cos\theta} \qquad \text{with } K = 0.94 \text{ (for spherical particles), the Scherrer constant;} \qquad (1)$$

λ = 0.154 nm, the applied X-ray wavelength;

β = FWHM;

ϑ = Bragg angle.

As mentioned above, the unordered structure makes amorphous rGO undetectable for XRD measurements. As a consequence, the calculated particle size *d* (**table S3**) only represents the particle size of the crystalline sLTO nanoparticles.

The average particle size of the respective samples was calculated by averaging the *hkl* particle size values (**table S3**).

Raman Spectroscopy (Raman)

Raman measurements were performed to study the changes of chemical bonding and analyse the purity of the synthesized sLTO/rGO-mixture. The Raman spectra were recorded at RT with a Bruker VIRTEX 70 spectrometer equipped with Bruker RAM II module (1064 nm laser) with nitrogen cooled Ge detector. The samples were measured in sealed glass pipettes in the region of 4000 to 80 cm^{-1} with a resolution of 4 cm^{-1}. Data processing was carried out with the software package OPUS 7.0.

The absence of weak characteristic peaks corresponding to the spinel LTO at 670 cm^{-1} (stretching vibration of Ti-O covalent bond) and 431 cm^{-1} (stretching vibration of Li-O ionic bond) can be explained by the overlapping with the strong RAMAN peaks of rGO.[21] In addition to the characteristic peaks of rGO discussed above, a third very intense peak at around 3200 cm^{-1} can be observed **in figure S5** (a). [22]

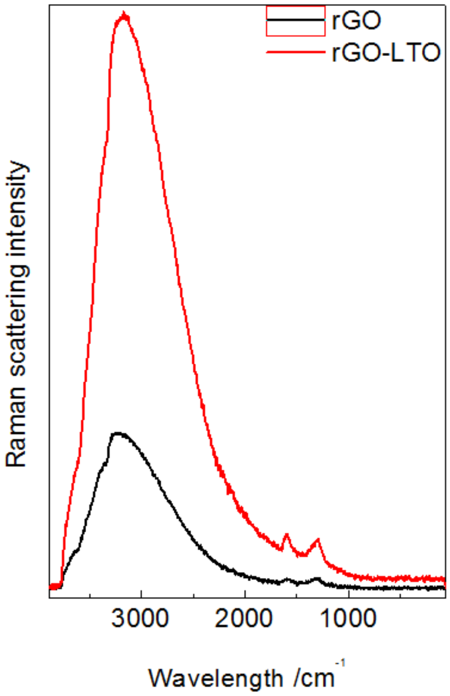

Figure S5: Complete Raman spectrum of rGO and the composite material.

This dominant 2D-band is also related to the amount of disordered *sp*^{3} carbon, but in contrast to the D-band presented above, the intensity of this peak is for example also correlated to the performance of the used laser. Therefore, this 2D-band isn’t a reliable source for further interpretation of the synthesized rGO, so that it wasn't considered in the analysis above.

Table S4: Summary of the characteristic rGO bands and the calculated intensity ratios for the curves represented in **figure S5** (c).

Route	**D-band / cm^{-1}**	**I_D / 10^{-3}**	**G-band / cm^{-1}**	**I_G / 10^{-3}**	$\frac{I_D}{I_G}$
(A)	1304	2.90	1597	2.53	1.146
(B)	1290	4.25	1590	3.31	1.284
(C)	1304	4.26	1594	3.43	1.242
(D)	1299	4.45	1590	3.35	1.328

The synthesized rGO/LTO composite (f**igure 2**) was investigated by Raman active rGO shows two characteristic main peaks, the so-called D- and G-bands, at around 1350 cm^{-1} and 1590 cm^{-1} respectively.[16,23] The intensity of the D-band is thereby proportional to the amount of disordered sp^3 carbon; and the intensity of the G-band proportional to the amount of ordered graphitic sp^2 carbon contained in the analysed sample.[16,23] These two correlations represent a possibility to determine the graphitization degree of the synthesized samples by calculating relative intensity ratio of these two bands $\left(\frac{\mathrm{I_D}}{\mathrm{I_G}}\right)$ (**table 13**). Low values for this ratio would mean that the graphitization degree is elevated, which lead to a better electrical conductivity.[16,22,24]

Attenuated Total Reflectance-Fourier Transform Infrared Spectroscopy (ATR-FTIR)

ATR-FTIR measurements were performed to study the changes of chemical bonding and analyse the purity of the synthesized sLTO/rGO-mixture. The ATR-FTIR spectra were recorded at RT with a PerkinElmer Spectrum Two IR spectrometer in the region of 4000 to 400 cm^{-1} with a resolution of 1 cm and a scan rate of 0.2 cm s^{-1}.

In this work, the ATR-FTIR spectroscopy was used to characterise the changes of functional groups in the reduction process of GO.[25,26] The changes would be observable by decreasing intensities of the oxygen functionalities contained in GO.[25] The corresponding characteristic peaks to these oxygen functionalities would appear at 3223 (O-H stretching), 1727 (C=O stretching), 1368 (O-H deformation), 1221 (epoxy C-O stretching) and 1046 cm^{-1} (alkoxy C-O stretching).[10,25,27–29]

Applying this knowledge on the synthesized LTO/rGO-composites, a weakening of the described oxygen related signals is expected to be observed in the ATR-FTIR- spectra. Especially for Route (B), this assumption could be proven due to the nearly completely disappeared signals at the characteristic positions mentioned above. Despite the identical reduction process for the Routes (B) and (C), a weaker decrease of the characteristic peaks can be observed for Route (C). Furthermore, the spectrum of Route (C) shows, in contrast to Route (B), an intense peak at around 3700 cm^{-1} most likely due to COOH-groups still contained in the reduced GO. As a consequence of the same observations for Route (D), it's assumed that the applied eco-friendly improved synthesis of graphene oxide provides higher oxidised GO than the traditional Hummer's method. The only difference in terms of chemicals used for the Routes (C) and (D) consists, as mentioned above, in the higher amount of the reducing agent L-AA used for the reduction of Route (D). The impact of this variation could be observed by a higher decrease of the characteristic peaks for Route (D) than for Route (C). By comparing all four curves in **Figure S6**, it especially seems like Route (A) still contains intercalated water leavings. An indication for the rightness of this assumption could be the small bumps at around 3350 cm^{-1} in the samples of Routes (B), (C) and (D); as well as the intense broad peak at the same position for Route (A). This peak can be related to O-H stretching vibrations in the water molecules.

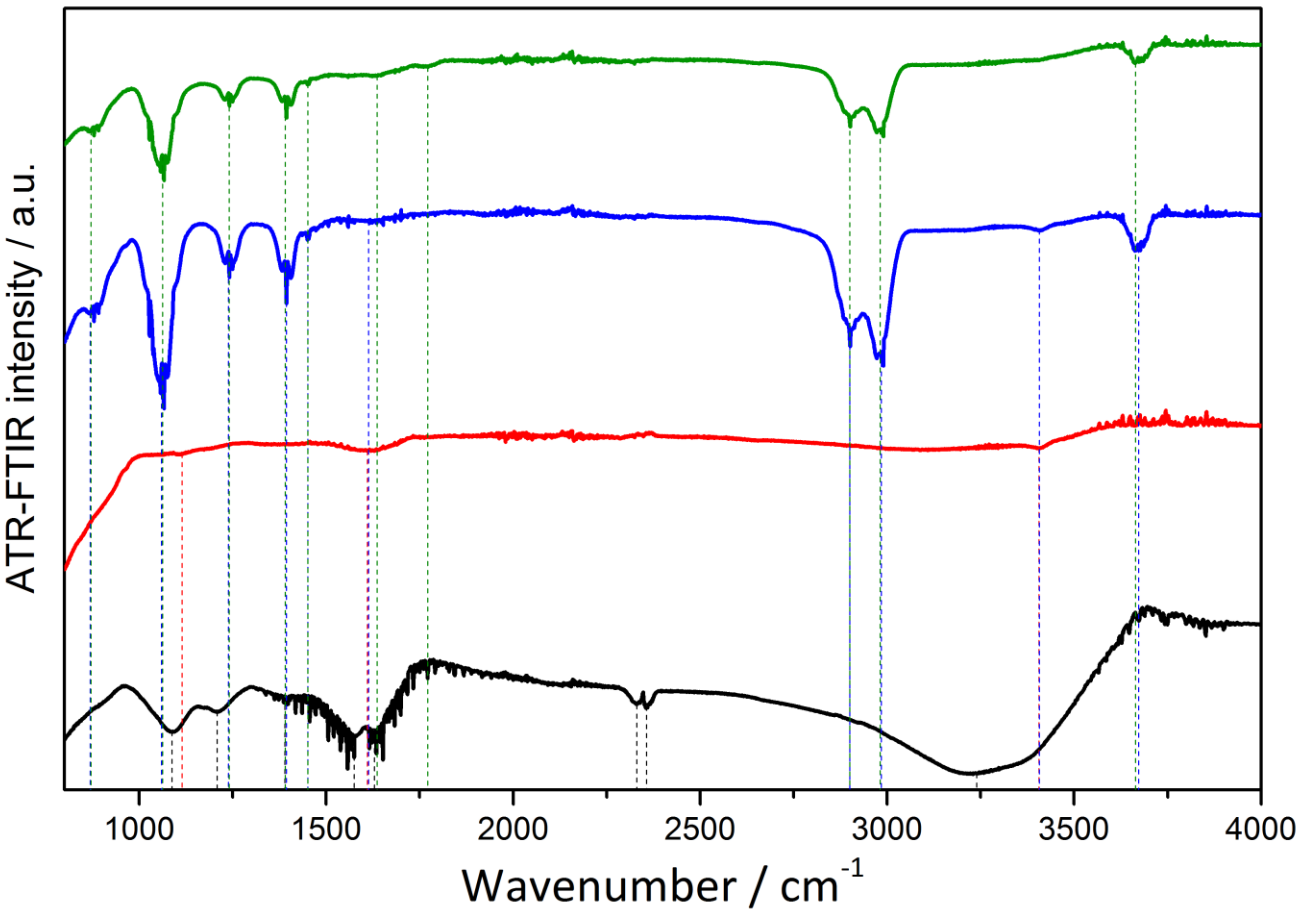

Figure S6: Determination of the characteristic ATR-FTIR peaks for Route (A) (black curve), Route (B) (red curve), Route (C) (blue curve) and Route (D) (green curve).

Table S5: Summary and interpretation of the observed peaks in **Figure S6 (b).**

Vibration	Route (A) / cm^{-1}	Route (B) / cm^{-1}	Route (C) / cm^{-1}	Route (D) / cm^{-1}
C-H deformation [30]	--	--	869	871
alkoxy C-O stretching [26,29–32]	1087	1115	1060	1062
epoxy C-O stretching [26,30,32,33]	1208	--	1239	1240
O-H deformation [26,29,31,32]	1389	--	1394	1391
C-OH stretching [30]	1574	--	1451	1451
C=C stretching [26,29,31,33]	1629	1610	1613	1636

C=O stretching [26,29–33]	--	--	--	1772
C-H deformation [30]	2331	--	--	--
C-H deformation [30]	2357	--	--	--
C-H stretching [30]	--	--	2900	2900
C-H stretching [30]	--	--	2984	2981
O-H stretching [26,29–33]	3239	3406	3406	--
O-H stretching	--	--	3672	3664

A characteristic peak of rGO can be observed for all four curves of **figure S6** at around 1620 cm^{-1}. This peak is originated in the C=C stretching vibrations and suggests that the sp^2 structure of the carbon atoms was remained. [25,30] The noise between 1300 cm^{-1} and 2400 cm^{-1} arise from the diamond crystal of the ATR-FTIR spectrometer.

Transmission Electron Microscopy (TEM)

TEM measurements were performed to examine fine details of the synthesized sLTO/rGO-mixture. The TEM images were recorded with a Carl Zeiss LEO 912 Omega instrument at an acceleration voltage of 120 kV. The samples for TEM were prepared by evaporating a small amount of ethanol solute LTO/rGO-composites onto a carbon-coated copper grid.

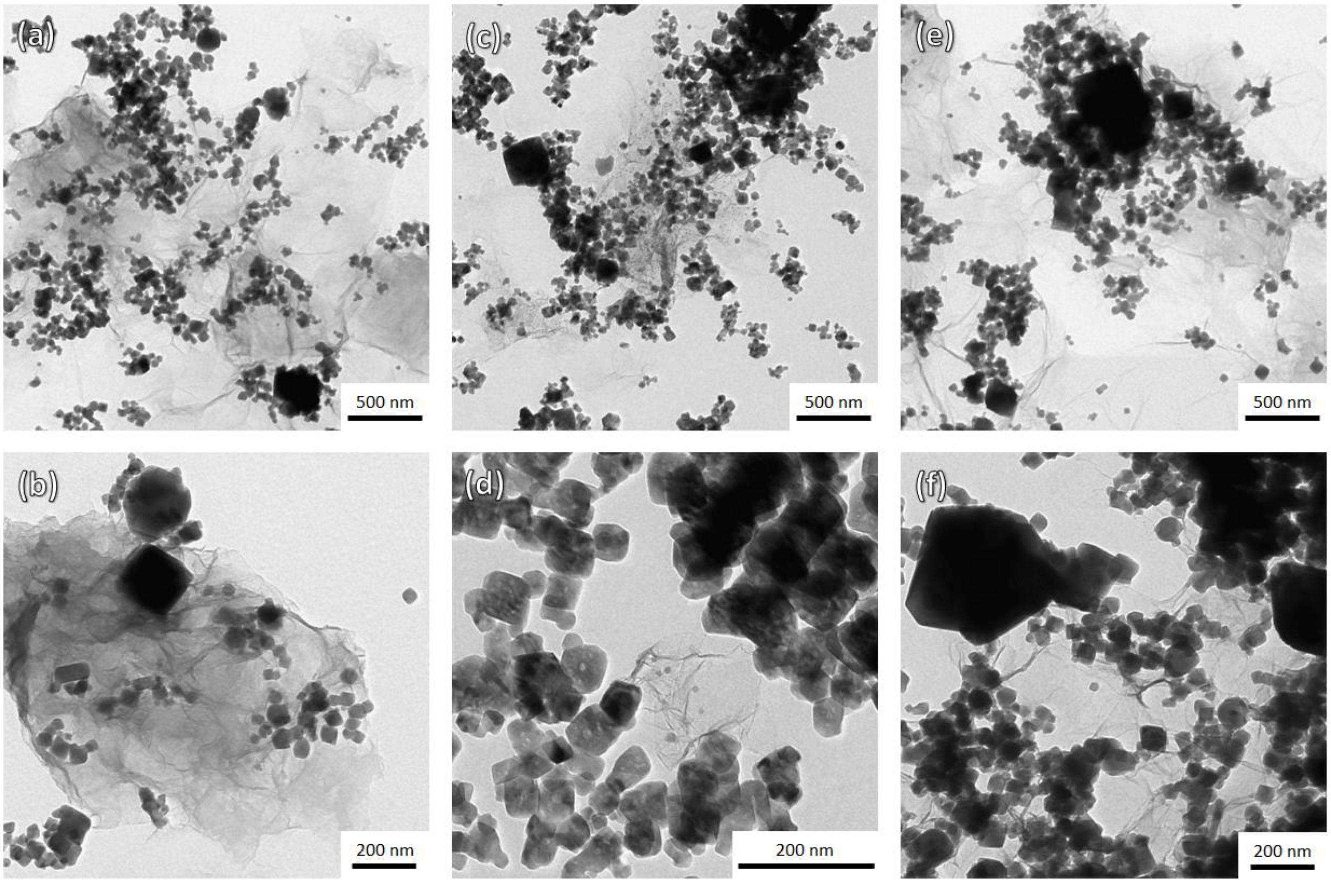

Figure S7: (a) & (b): TEM images of Route (A) at different resolutions. (c) & (d): TEM images of Route (B) at different resolutions. (e) & (f): TEM images of Route (C) at different resolutions.

In **Figure S7 (**a), (c) and (e), it could be shown that, especially for Route (A), the sLTO nanoparticles are well-dispersed on the rGO nanosheets. This observation proved the assumption that the insertion of rGO would lead to an extenuated agglomeration of the sLTO nanoparticles. [9,16] By analysing the presented TEM images in detail, the positive impact of sonication on the homogeneous distribution of rGO could also be visualized. For example, it looks like the rGO distribution in Route (C) (**Figure S7 (**e)) is less homogeneous than in the sonicated Route (A) (**Figure S7 (a**)), resulting in a higher tendency of agglomeration for Route (C). In **Figure S7** (b), (d) and (f) the porous structure of the crystalline sLTO nanoparticles as well as a high quantity of rGO based pore channels between the different nanoparticles have been visualized. In theory, this elevated porosity of the samples should lead to shorter transfer paths of electrons and Li$^+$ ions; resulting in an improved capacity and rate capability of the samples. [16]

SEM Results

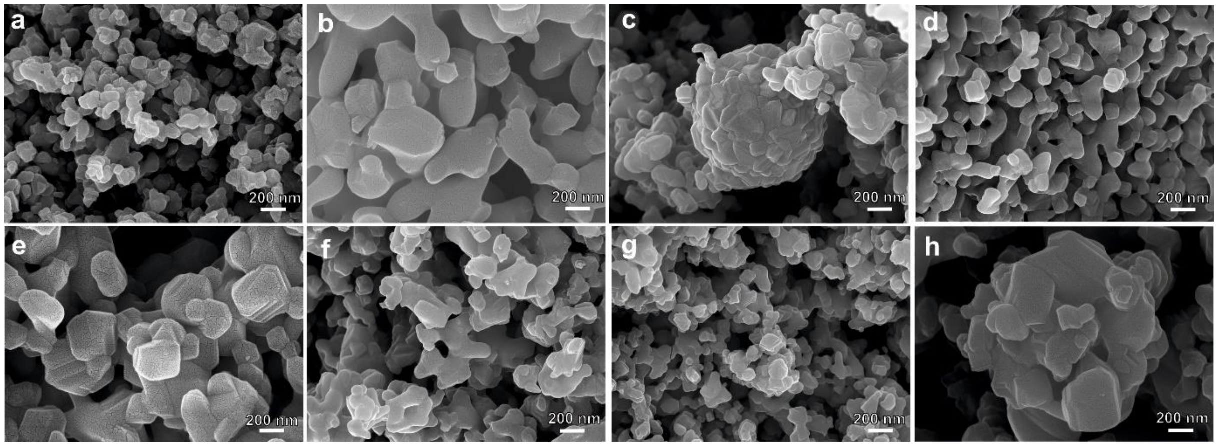

Figure S8. FE-SEM images of undoped $Li_4Ti_5O_{12}$ (a) and Fe doped $Li_4Ti_5O_{12}$ NPs 0.001% Fe^{3+} (b), 0.01% Fe^{3+} (c), 0.1% Fe^{3+} (d), 0.5% Fe^{3+} (e), 1% Fe^{3+} (f), 2% Fe^{3+} (g), 5% Fe^{3+} (h).

Electrochemical Impedance Spectroscopy (EIS)

Nyquist plot

The data acquired by an EIS measurement can be described by a Nyquist plot (**figure S9**). In a Nyquist plot, the frequency responses of linear systems are represented in a complex plot. The x-axis represents the real part of the complex impedance value and is a measure for the dissipated energy in the sample. The y-axis represents the imaginary part of the complex resistivity and is a measure for the stored energy in the sample. [34] Briefly, a Nyquist plot describes the impedance of a material. In **figure S9**, a Nyquist plot is shown theoretically. Φ is the phase angle between the real part and the vector measuring $|Z|$, i.e. the amplitude of the measured impedance at a definite frequency. However, it is impossible to identify the used frequency to record one point by just looking at that one data point. Usually, low frequency data are on the right and high frequency data on the left side of the Nyquist plot.

With the EIS analysis, it is possible to calculate the capacitance of the system. With decreasing radius of the semicircle, the impedance also decreases and the conductivity increases. When the underlying equivalent circuit model is chosen, the model's parameters are usually fitted by the aid of a fitting program (in present case: Zview, Scribner Associates Inc.).

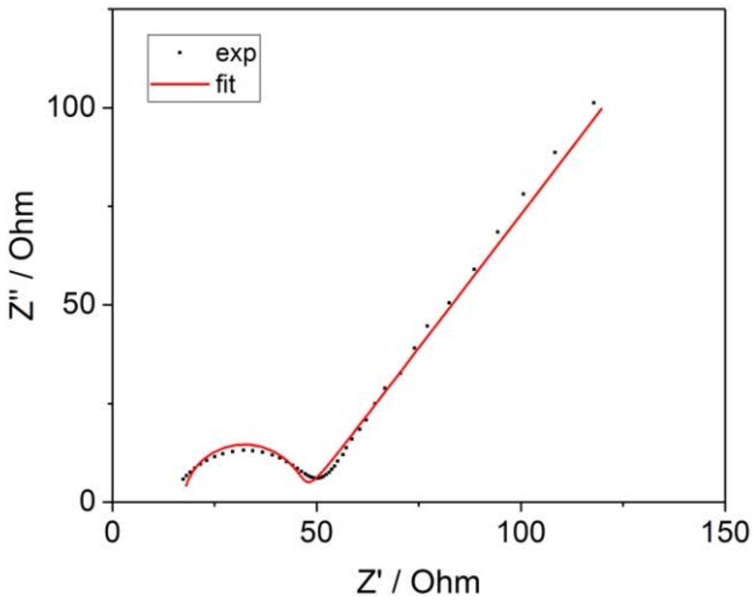

Figure S9: Nyquist plot for a pure sLTO anode, EIS parameter: *I* = 10 mA, frequency range: 10 MHz to 0.1 Hz.

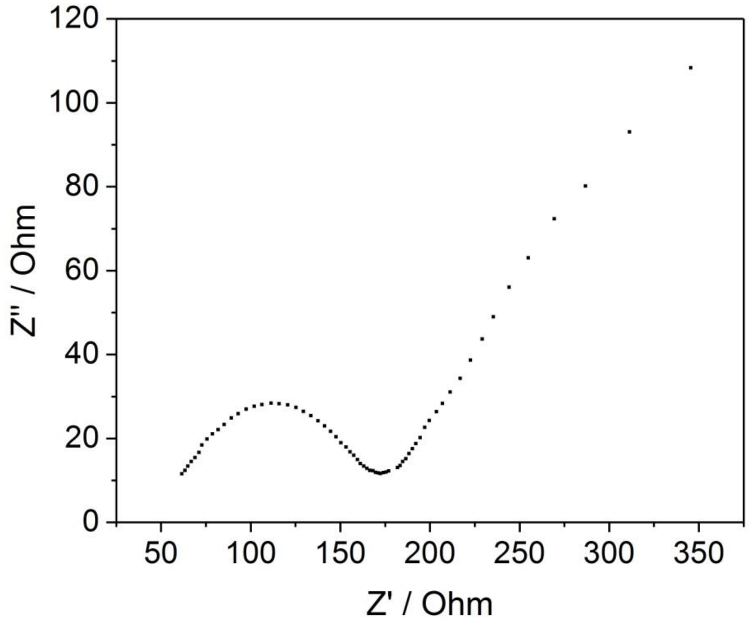

Figure S10: Nyquist plot for a pure rGO anode, EIS parameter: *I* = 10 mA, frequency range: 10 MHz to 0.1 Hz.

Equivalent circuits

The composition of the equivalent circuits depends on the reactions taking place in the considered electrochemical cell. One important element is the solution resistance (R_S), which may depend e.g. on the ionic concentration of the ionic solution. It is usually in series with a capacitance, which describes the ability of a system to store an electrical charge. In the present case, the capacitance is called the double layer capacitance (C_{DL}). Another resistance is the charge transfer resistance (R_{CT}) which results from an electron transfer from one phase (e.g. electrode) to another (e.g. liquid). The Warburg element (W) models the diffusion process, and is nearly always associated with a double layer capacitance. It only appears at smaller frequencies ω, because of the proportionality to $\frac{1}{\sqrt{\omega}}$. In a Nyquist plot, it is characterized by a diagonal line with a slope of 45°. [35] A constant phase element (CPE) explains the impedance response by means of the Young resistivity distribution. [16] The mostly used circuit is the Randles cell [17] (**figure S11**), which includes a solution resistance, a Warburg element, a double layer capacitance and a charge transfer resistance.

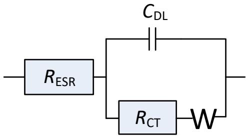

Figure S11: Drawing of a Randles circuit model.

References

(1) Hummers, W. S.; Offeman, R. E. Preparation of Graphitic Oxide. *Journal of the American Chemical Society* **1958**, *80*, 1339.

(2) Fathy, M.; Gomaa, A.; Taher, F. A.; El-Fass, M. M.; Kashyout, A. E.-H. B. Optimizing the Preparation Parameters of GO and rGO for Large-Scale Production. *Journal of Materials Science* **2016**, *51*, 5664–5675.

(3) Pielaszek, R. Diffraction studies of microstructure of nanocrystals exposed to high pressure. Ph. D. Thesis, Warsaw University, Warsaw, 2003.

(4) Otto, M. *Analytische Chemie*, 4. Überarbeitete und Ergänzte Auflage; Wiley-VCH Verlag GmbH & Co. KGaA: Weinheim, Germany, 2011.

(5) Marciano, O.; Gonen, S.; Levy, N.; Teblum, E.; Yemini, R.; Nessim, G. D.; Ruthstein, S.; Elbaz, L. Modulation of Oxygen Content in Graphene Surfaces Using Temperature-Programmed Reductive Annealing: Electron Paramagnetic Resonance and Electrochemical Study. *Langmuir: The ACS Journal of Surfaces and Colloids* **2016**, *32*, 11672–11680.

(6) Dellinger, B.; Lomnicki, S.; Khachatryan, L.; Maskos, Z.; Hall, R. W.; Adounkpe, J.; McFerrin, C.; Truong, H. Formation and Stabilization of Persistent Free Radicals. *Proceedings of the Combustion Institute. International Symposium on Combustion* **2007**, *31*, 521–528.

(7) Kausteklis, J.; Cevc, P.; Arčon, D.; Nasi, L.; Pontiroli, D.; Mazzani, M.; Riccò, M. Electron Paramagnetic Resonance Study of Nanostructured Graphite. *Physical Review B* **2011**, *84*.

(8) Pol, S. V.; Pol, V. G.; Gedanken, A. Encapsulating ZnS and ZnSe Nanocrystals in the Carbon Shell: A RAPET Approach. *The Journal of Physical Chemistry C* **2007**, *111*, 13309–13314.

(9) Chen, C.; Huang, Y.; Zhang, H.; Wang, X.; Li, G.; Wang, Y.; Jiao, L.; Yuan, H. Small Amount of Reduce Graphene Oxide Modified $Li_4Ti_5O_{12}$ Nanoparticles for Ultrafast High-Power Lithium Ion Battery. *Journal of Power Sources* **2015**, *278*, 693–702.

(10) Marcano, D. C.; Kosynkin, D. V.; Berlin, J. M.; Sinitskii, A.; Sun, Z.; Slesarev, A.; Alemany, L. B.; Lu, W.; Tour, J. M. Improved Synthesis of Graphene Oxide. *ACS Nano* **2010**, *4*, 4806–4814.

(11) Stankovich, S.; Dikin, D. A.; Piner, R. D.; Kohlhaas, K. A.; Kleinhammes, A.; Jia, Y.; Wu, Y.; Nguyen, S. T.; Ruoff, R. S. Synthesis of Graphene-Based Nanosheets via Chemical Reduction of Exfoliated Graphite Oxide. *Carbon* **2007**, *45*, 1558–1565.

(12) Fernández-Merino, M. J.; Guardia, L.; Paredes, J. I.; Villar-Rodil, S.; Solís-Fernández, P.; Martínez-Alonso, A.; Tascón, J. M. D. Vitamin C Is an Ideal Substitute for Hydrazine in the Reduction of Graphene Oxide Suspensions. *The Journal of Physical Chemistry C* **2010**, *114*, 6426–6432.

(13) Lai, Q.; Zhu, S.; Luo, X.; Zou, M.; Huang, S. Ultraviolet-Visible Spectroscopy of Graphene Oxides. *AIP Advances* **2012**, *2*, 32146.

(14) Yoon, S.-B.; Kim, H.-K.; Roh, K. C.; Kim, K.-B. Electrochemical Kinetics Investigation of $Li_4Ti_5O_{12}$/Reduced Graphene Oxide Nanocomposite Using Voltammetric Charge Analysis. *Journal of The Electrochemical Society* **2015**, *162*, A667-A673.

(15) Cava, R. J.; Murphy, D. W.; Zahurak, S.; Santoro, A.; Roth, R. S. The Crystal Structures of the Lithium-Inserted Metal Oxides $Li_{0.5}TiO_2$ anatase, $LiTi_2O_4$ spinel, and $Li_2Ti_2O_4$. *Journal of Solid State Chemistry* **1984**, *53*, 64–75.

(16) Chen, W.; Jiang, H.; Hu, Y.; Dai, Y.; Li, C. Mesoporous Single Crystals $Li_4Ti_5O_{12}$ Grown on rGO as High-Rate Anode Materials for Lithium-Ion Batteries. *Chemical Communications* **2014**, *50*, 8856–8859.

(17) Liu, H.-p.; Wen, G.-w.; Bi, S.-f.; Wang, C.-y.; Hao, J.-m.; Gao, P. High Rate Cycling Performance of Nanosized $Li_4Ti_5O_{12}$/Graphene Composites for Lithium Ion Batteries. *Electrochimica Acta* **2016**, *192*, 38–44.

(18) Uvarov, V.; Popov, I. Metrological Characterization of X-Ray Diffraction Methods for Determination of Crystallite Size in Nano-Scale Materials. *Materials Characterization* **2007**, *58*, 883–891.

(19) Shull, C. G. The Determination of X-Ray Diffraction Line Widths. *Physical Review* **1946**, *70*, 679–684.

(20) Wedler, G.; Freund, H.-J. *Lehrbuch der Physikalischen Chemie*, Sechste, vollständig überarbeitete und aktualisierte Auflage; Wiley-VCH Verlag GmbH & Co. KGaA: Weinheim, 2012.

(21) Xu, G.; Tian, Y.; Wei, X.; Yang, L.; Chu, P. K. Free-Standing Electrodes Composed of Carbon-Coated $Li_4Ti_5O_{12}$ Nanosheets and Reduced Graphene Oxide for Advanced Sodium Ion Batteries. *Journal of Power Sources* **2017**, *337*, 180–188.

(22) Chen, Y.; Fu, K.; Zhu, S.; Luo, W.; Wang, Y.; Li, Y.; Hitz, E.; Yao, Y.; Dai, J.; Wan, J.; Danner, V. A.; Li, T.; Hu, L. Reduced Graphene Oxide Films with Ultrahigh Conductivity as Li-Ion Battery Current Collectors. *Nano Letters* **2016**, *16*, 3616–3623.

(23) Khan, A.; Wang, J.; Li, J.; Wang, X.; Chen, Z.; Alsaedi, A.; Hayat, T.; Chen, Y.; Wang, X. The Role of Graphene Oxide and Graphene Oxide-Based Nanomaterials in the Removal of Pharmaceuticals from Aqueous Media: A Reiew: A Review. *Environmental Science and Pollution Research International* **2017**, *24*, 7938–7958.

(24) Li, B.; Han, C.; He, Y.-B.; Yang, C.; Du, H.; Yang, Q.-H.; Kang, F. Facile Synthesis of $Li_4Ti_5O_{12}$/C Composite with Super Rate Performance. *Energy & Environmental Science* **2012**, *5*, 9595.

(25) Xu, C.; Shi, X.; Ji, A.; Shi, L.; Zhou, C.; Cui, Y. Fabrication and Characteristics of Reduced Graphene Oxide Produced with Different Green Reductants. *PloS one* **2015**, *10*, e0144842.

(26) Chen, D.; Feng, H.; Li, J. Graphene Oxide: Preparation, Functionalization, and Ectrochemical Applications. *Chemical Reviews* **2012**, *112*, 6027–6053.

(27) Zhang, J.; Yang, H.; Shen, G.; Cheng, P.; Zhang, J.; Guo, S. Reduction of Graphene Oxide via L-Ascorbic Acid. *Chemical Communications* **2010**, *46*, 1112–1114.

(28) Zhu, C.; Guo, S.; Fang, Y.; Dong, S. Reducing Ssugar: New Functional Molecules for the Green Synthesis of Graphene Nanosheets. *ACS Nano* **2010**, *4*, 2429–2437.

(29) Kong, D.; Le, L. T.; Li, Y.; Zunino, J. L.; Lee, W. Temperature-Dependent Electrical Properties of Graphene Inkjet-Printed on Flexible Materials. *Langmuir: The ACS Journal of Surfaces and Colloids* **2012**, *28*, 13467–13472.

(30) Su, X.; Wang, G.; Li, W.; Bai, J.; Wang, H. A Simple Method for Preparing Graphene Nano-Sheets at Low Temperature. *Advanced Powder Technology* **2013**, *24*, 317–323.

(31) Allahbakhsh Ahmad; Sarif, F.; Mazinani, S. The Influence of Oxygen-Containing Functional Groups on the Surface Behavior and Roughness Characteristics of Graphene Oxide. *Nano* **2013**, *08*, 1350045.

(32) Mermoux, M.; Chabre, Y.; Rousseau, A. FTIR and 13C NMR study of graphite oxide. *Carbon* **1991**, *29*, 469–474.

(33) Perkampus, H.-H. *UV-VIS Spectroscopy and Its Applications*; Springer Lab Manuals; Springer Berlin Heidelberg: Berlin, Heidelberg, 1992.

(34) Momma, T.; Matsunaga, M.; Mukoyama, D.; Osaka, T. Ac Impedance Analysis of Lithium Ion Battery Under Temperature Control. *Journal of Power Sources* **2012**, *216*, 304–307.

(35) Taylor, S. R.; Gileadi, E. Physical Interpretation of the Warburg Impedance. *Corrosion* **1995**, *51*, 664–671.